# Plug-and-Play for Joint Deblurring and Guided Super-Resolution of Single-Photon 3D Lidar data

Abderrahim Halimi, and Stephen McLaughlin
School of Engineering and Physical Sciences, Heriot-Watt University, Edinburgh UK

***Abstract*—This paper presents a new method for joint deblurring and super-resolution of 3D single-photon Lidar images. Adopting a plug-and-play framework, the method alternates between a data fidelity iterate, and a guided filtering (GF) step which can be performed by any existing GF algorithm. The resulting analytical updates are efficient and are easily adapted to different upscaling factors or arbitrary blur kernels. Thanks to the GF algorithm, the algorithm shows good denoising performance when imaging in extreme conditions leading to high background noise. Experiments on simulated and real data demonstrate the good performance of the proposed strategy in terms of depth maps deblurring and super-resolution in presence of high levels of noise.**

***Index Terms*—3D Reconstruction, Single-Photon Imaging, Lidar, Deblurring, Super-Resolution, Plug-and-PLay.**

## I. Introduction

3D imaging with single-photon Lidar (SPL) systems is an emerging technology with an increasing impact in several applications [1], [2]. SPL operates by sending light pulses and detecting the reflected photons while measuring their time-of-flight, which contain target's depth and reflectivity information. Recent technological advances have shown increasing use of sensor SPAD arrays (single-photon avalanche diodes) which enable parallel scanning of multiple pixels, hence enabling fast imaging. However, the arrays are often small leading to low-resolution depth images. Imaging in extreme conditions also affects the quality of measured data. Indeed, imaging through obscurants [3]–[5] (e.g., fog, underwater) or in bright conditions increase the noise background, while imaging at long range (km-range) [6] or fast moving objects might introduce an X-Y spatial blur. These limitations highlight the need for an advanced processing strategy to deliver high quality depth estimates.

Several reconstruction methods have been designed to tackle these challenges. A focus has been on designing denoising methods [4], [7]–[11] exploiting data statistics and spatial correlations to recover clean 3D information. Improving the spatial resolution of Lidar data also investigated using statistical methods [5], or deep-leaning (DL) methods such as [12]–[14]. However, these DL methods require re-training the model for each imaging system (e.g. due to different impulse response or imaging conditions), or when changing the upscaling factor. Few methods have also tackled the motion blur affecting single-photon data when imaging fast moving objects [15] or for long range imaging as in [16].

This paper proposes a new plug-and-play (PnP) algorithm for joint deblurring and guided super-resolution of SPL depth and reflectivity images. The method alternates between a data fidelity step and guided filter (GF) step. The latter can be performed by any existing GF algorithm, as introduced in the PnP framework [17]. In this paper, we considered the guided image filter (GIF) from [18] as it leads to efficient analytical updates. The proposed method can be used with different upscaling factors and accounts for arbitrary but known blur kernels that can result from motion or long-range imaging. Results on simulated and real data confirm the performance of the proposed method for denoising, deblurring and super-resolution.

The paper is organized as follows. Section II introduces the observation model and corresponding challenges. The proposed method is then introduced in Section III. Results on simulated and real data are presented in Sections IV and V. Conclusions and future are finally reported in Section VI.

## II. Problem statement

### A. Approximate Lidar observation model

The photons detected by a single photon Lidar system are usually collected into a histogram of counts with respect to their TOFs. Denoting $y_{n,t}$ the histogram at the $n$th pixel for the $t$th time of flight, it is usually assumed to follow a Poisson distribution $\mathcal{P}(.)$ as follows

$$y_{n,t} \sim \mathcal{P}\left(x_{n,t}\right), \text{ with } x_{n,t} = r_n\, h\left(t - d_n\right) + b_{n,t}, \qquad (1)$$

where we assume the presence of a single target's peak per pixel with $r_n$ denoting the target's reflectivity, $d_n$ the target's depth, $h$ the system impulse response function (IRF), and $b_{n,t}$ the background of counts due to the environment. In what follows, we assume a normalized IRF: $\sum_{t=1}^{T} h\left(t - d_n\right) = 1$ with the total number of bins $T$ and independent observations with respect to different pixels, leading to

$$p\left(\boldsymbol{Y} \mid \boldsymbol{d}, \boldsymbol{r}\right) = \prod_{n=1}^{N} \prod_{t=1}^{T} p\left(y_{n,t} \mid d_n, r_n\right), \qquad (2)$$

with $\boldsymbol{d} = \{d_n\}$ and $\boldsymbol{r} = \{r_n\}$ are $N \times 1$ vectors. Our goal is to estimate high-resolution depth parameter from these observations. A common strategy to obtain efficient estimators is to approximate the likelihood term [4], [19], and to enforce regularization constraints to the resulting estimation problem.

This work was supported by the UK Royal Academy of Engineering under the Research Fellowship Scheme (RF/201718/17128) and EPSRC Grants EP/T00097X/1,EP/S026428/1.

In what follows, we approximate the Poisson likelihood with a Gaussian distribution [20]. This is a valid approximation for recent SPAD array sensors [21], [22] operating in the dense photon regime (although we will show in experiments that the proposed model also provides good results in the sparse photon case). Also, it is common to assume the absence of the background or a pre-processing step removing it, in which case the maximum likelihood estimate $\hat{d}_n$ of the depth reduces to a matched filter

$$\hat{d}_n\left(\boldsymbol{y}_n\right) = \max_d \left\{ \sum_t y_{n,t} h(t-d) \right\} = \max_d \left\{ \boldsymbol{y}_n \otimes_t \boldsymbol{h}(d) \right\} \tag{3}$$

where $\otimes_t$ denotes a temporal cross-correlation and $\boldsymbol{h}$ denotes the impulse response function. The reflectivity maximum likelihood estimate can be obtained as the sum of photons around the detected peak.

### B. Challenges

Recent advances in single-photon technology have allowed the development of SPAD arrays, enabling fast imaging. However, current arrays often have a limited number of pixels, which leads to low resolution images. In addition, real-world applications involve long-range imaging where the laser beam might cover multiple pixels, and imaging of fast moving objects compared to the imaging speed. Both result in blurry images due to the convolution of the point returns with a X-Y spatial kernel. This affects the observation model that can be written as

$$\boldsymbol{y}_{:t} = \left(\boldsymbol{x}_{:t} \otimes \boldsymbol{k}\right) \downarrow_s + \boldsymbol{e} \tag{4}$$

where $\boldsymbol{y}_{:t}$ is the vector of counts at all pixels for the $t$th time bin, $\boldsymbol{x}_{:t}$ represents the high-resolution image, $\boldsymbol{k}$ is an spatial blur kernel, $\otimes$ denotes the circular spatial convolution, $\downarrow_s$ is a spatial downsampling by $s$ and $\boldsymbol{e} \sim \mathcal{N}(0, \eta_n)$ is a Gaussian noise, with $\eta_n = \eta$ a noise variance independent of $\boldsymbol{x}$. In this paper, we adopt a joint super-resolution and deblurring strategy to enhance the resolution of the resulting images, sharpen the observed depth images and recover small features. In what follows, we drop the index in $\boldsymbol{y}_{:t}$ for simplicity, but operations should be understood to be applied to each $t$th frame.

## III. Proposed method

### A. Plug-and-Play framework

The high-resolution image $\boldsymbol{x}$ can be estimated by minimizing the regularized negative log-likelihood as follows

$$\min_x ||\boldsymbol{y} - \left(\boldsymbol{x} \otimes \boldsymbol{k}\right) \downarrow_s ||^2 + \lambda \phi(\boldsymbol{x}) \tag{5}$$

where $\phi(\boldsymbol{x})$ is a regularization term enforcing suitable structure for $\boldsymbol{x}$. In the deep image prior framework [23], it was shown that modelling $\boldsymbol{x}$ using a neural network provides a good prior as follows

$$\min_{\boldsymbol{\theta}} ||\boldsymbol{y} - \left[f_{\boldsymbol{\theta}}(\boldsymbol{g}) \otimes \boldsymbol{k}\right] \downarrow_s ||^2 + \epsilon \psi(\boldsymbol{\theta}) \tag{6}$$

where $f_{\boldsymbol{\theta}}(\boldsymbol{g})$ is a non-linear function depending on parameters $\boldsymbol{\theta}$, and a guiding image $\boldsymbol{g}$. In this paper, we adopt the half-quadratic splitting algorithm that introduces a latent variable $\boldsymbol{z}$ leading to

$$\min_{\boldsymbol{\theta},\boldsymbol{z}} ||\boldsymbol{y} - \left(\boldsymbol{z} \otimes \boldsymbol{k}\right) \downarrow_s ||^2 + \mu ||\boldsymbol{z} - f_{\boldsymbol{\theta}}(\boldsymbol{g})||^2 + \epsilon \psi(\boldsymbol{\theta}). \tag{7}$$

Minimizing this cost function alternates between minimization of an $\ell_2 - \ell_2$ term to update $\boldsymbol{z}$

$$\min_{\boldsymbol{z}} ||\boldsymbol{y} - \left(\boldsymbol{z} \otimes \boldsymbol{k}\right) \downarrow_s ||^2 + \mu ||\boldsymbol{z} - f_{\boldsymbol{\theta}}(\boldsymbol{g})||^2, \tag{8}$$

and the term

$$\min_{\boldsymbol{\theta}} \mu ||\boldsymbol{z} - f_{\boldsymbol{\theta}}(\boldsymbol{g})||^2 + \epsilon \psi(\boldsymbol{\theta}). \tag{9}$$

which is the guided filtering of $\boldsymbol{z}$ using the guidance $\boldsymbol{g}$. Under the PnP, this step can be replaced by any state-of-the-art guided filter.

### B. Proposed model for efficient inference

In this paper, we aim for efficient inference that can be implemented on-chip in imaging sensors. Therefore, we propose to consider the guided image filtering model [18] to represent $f_{\boldsymbol{\theta}}(\boldsymbol{g})$. More precisely, this model assumes the filtered image is a linear transformation of $\boldsymbol{g}$, with coefficients $\boldsymbol{\theta} = (\boldsymbol{a}, \boldsymbol{b})$, in a $w \times w$ window $\omega_n$ centered at the $n$th pixel. Model (7) reduces to

$$\begin{aligned} \min_{\boldsymbol{a},\boldsymbol{b},\boldsymbol{z}} \quad & ||\boldsymbol{y} - \left(\boldsymbol{z} \otimes \boldsymbol{k}\right) \downarrow_s ||^2 + \\ & \mu \sum_{n=1}^{N} \left[ \sum_{i \in \omega_n} \left(a_n g_i + b_n - z_i\right)^2 + \epsilon a_n^2 \right] \end{aligned} \tag{10}$$

which can be expressed as

$$\min_{\boldsymbol{a},\boldsymbol{b},\boldsymbol{z}} ||\boldsymbol{y} - \left(\boldsymbol{z} \otimes \boldsymbol{k}\right) \downarrow_s ||^2 + \mu ||\boldsymbol{z} - \boldsymbol{x}(\boldsymbol{a}, \boldsymbol{b}, \boldsymbol{g})||^2 + \epsilon ||\boldsymbol{a}||^2. \tag{11}$$

Interestingly, the iterative updates in (9) can be analytically obtained. The $\ell 2$-$\ell 2$ minimization problem w.r.t. $\boldsymbol{z}$ can be efficiently solved in the FFT domain as in [24], [25]

$$\boldsymbol{z} = \mathcal{F}^{-1}\left[ \frac{1}{\mu} \left( \boldsymbol{d} - \overline{\mathcal{F}(\boldsymbol{k})} \odot_s \frac{\left(\mathcal{F}(\boldsymbol{k}) \boldsymbol{d}\right) \Downarrow_s}{\left(\overline{\mathcal{F}(\boldsymbol{k})} \mathcal{F}(\boldsymbol{k})\right) \Downarrow_s + \mu} \right) \right] \tag{12}$$

where $\boldsymbol{d} = \overline{\mathcal{F}(\boldsymbol{k})} \mathcal{F}(\boldsymbol{y} \uparrow_s) + \mu \mathcal{F}(\boldsymbol{x})$, the FFT, inverse FFT operators are denoted by $\mathcal{F}, \mathcal{F}^{-1}$ and $\overline{\mathcal{F}}$ is the complex conjugate of $\mathcal{F}$, $\odot_s$ represents element-wise multiplication to the s × s distinct blocks of $\overline{\mathcal{F}(\boldsymbol{k})}$, $\Downarrow_s$ is the block downsampler by averaging the s × s distinct blocks, $\uparrow_s$ is s-fold upsampler by filling the new entries with zeros.

The minimization problems w.r.t. $\boldsymbol{a}$ and $\boldsymbol{b}$ can also be solved analytically as in [18]

$$x_n = \frac{\left(\sum_{i \in \omega_n} a_i\right) g_n + \left(\sum_{i \in \omega_n} b_i\right)}{|\omega|}, \forall n \tag{13}$$

where $|\omega|$ is the number of pixels in $\omega_n$,

$$a_i = \frac{\frac{1}{|\omega|} \left(\sum_{j \in \omega_i} g_j z_j\right) - m_i \bar{z}_i}{\sigma_i^2 + \epsilon}, \text{ and } b_i = \bar{z}_i - a_i m_i \tag{14}$$

where $m_i, \sigma_i^2$ are the mean and variance of $\boldsymbol{g}$ in $\omega_i$, and $\bar{z}_i$ is the mean of $\boldsymbol{z}$ in $\omega_i$. This shows that all updates are analytical allowing fast inference of these parameters. After these updates, the depth map is estimated as in (3). Note here that the guidance is applied to the histogram of counts instead of directly applying it to the depth map, hence reducing texture transfer issues as observed when applying guided image filtering on the depth map. Algo. 1 summarizes the main steps of the overall deblurring and super-resolution 3D (DS3D) filtering approach.

**Algorithm 1** DS3D - guided super-resolution method

1: Input: Lidar data $\boldsymbol{Y}$, IRF: $\boldsymbol{h}$, guidance: $\boldsymbol{g}$
2: **while** conv$= 0$ **do**
3: Update $\boldsymbol{z}$ analytically using (12) as in [24], [25]
4: Update $\boldsymbol{x}$ analytically using (13) as in [18]
5: **end while**
6: Compute $\hat{\boldsymbol{d}}(\boldsymbol{z})$ as in (3)
7: Output: $\boldsymbol{z}, \boldsymbol{x}, \hat{\boldsymbol{d}}$

## IV. Results on simulated data

The performance of the proposed algorithm is evaluated on simulated data by considering three aspects: denoising, deblurring and super-resolution. We first introduce the considered data, comparison algorithms and evaluation criteria. Then, we describe the results obtained regarding each aspect. All simulations were performed on a Matlab R2021a on a computer with Intel(R) Xeon(R) Gold 6230 CPU @ 2.10GHz and 128GB RAM.

### A. Data, algorithms and evaluation criteria

The $555 \times 695$ depth and intensity images of the art scene (see [26]) are used to simulate Lidar data according to the model in (1). The resulting histograms of counts have $T = 300$ time bins (with 20ps per time bin), and use a real system impulse response (leading-edge of 3 bins and trailing-edge of 26 bins). We considered different levels of signal-to-background ratio (SBR$= \frac{\sum_{n=1}^{N} r_n}{\sum_{n=1}^{N}\sum_{t=1}^{T} b_{n,t}}$) and average photon-per-pixel PPP$= 1/N \sum_{n=1}^{N}\sum_{t=1}^{T} x_{n,t}$. Fig. 2 (left) shows the reference point cloud. The proposed deblurring and super-resolution 3D algorithm (denoted DS3D) is compared to several algorithms, i.e., the classical maximum-likelihood algorithm, the unmixing algorithm (UA) [27] and the multiscale Bayesian 3D reconstruction (MB3D) algorithm [4]. The performance is evaluated qualitatively by visualizing the reconstructed depth images and point clouds and quantitatively using the depth absolute error ($\ell_1$ error between the ground-truth and reconstructed depth maps).

### B. Depth denoising

This section evaluates the denoising capabilities of the proposed algorithm. Note that DS3D was not designed to perform this task, however, the iterative guided filtering step improves the quality of the processed histograms, hence allowing an improved depth estimation and outliers rejection. In this part, we assume the absence of a blur kernel and set the downsampling factor to $s = 1$. Fig. 1 shows the obtained DAE results when considering the Class., UA, MB3D and the proposed DS3D algorithms. As expected, the classical algorithm shows the worst performance. The DS3D shows good results even at extreme SBR and PPP levels. The DS3D shows better performance than the UA algorithm, and compares well with the denoising MB3D algorithm.

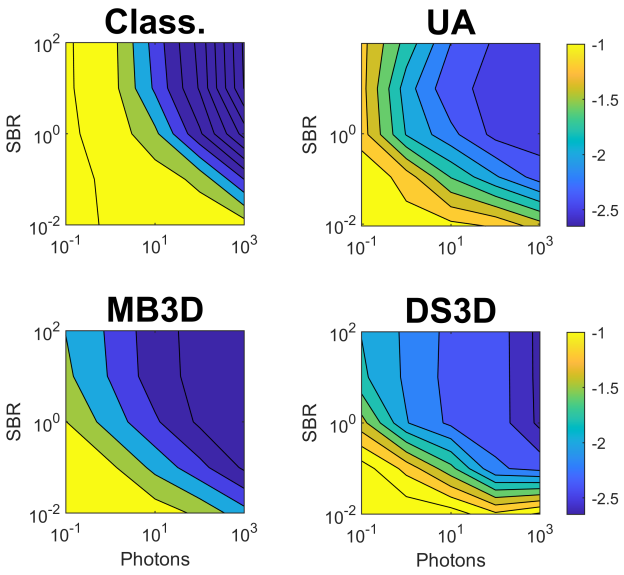


Fig. 1. Depth Absolute Error (DAE) in log scale for different levels of SBR and PPP and several algorithms, i.e., Classical, UA [27], MB3D [4], and proposed DS3D algorithms.

### C. Joint depth super-resolution and deblurring

In contrast to deep-learning super-resolution methods [13], [14] that require re-training for each upscaling factor $s$, the DS3D generalizes well to different $s$. In addition, it can also account for arbitrary blurring kernels due to sensor low-resolution or motion blur. To highlight these aspects, we evaluated DS3D by considering two scaling factors $s = \{4, 8\}$ and considered two blurring kernels, a uniform kernel to simulate a macro pixel in low-resolution sensors, and one arbitrary kernel (although other kernels can be easily studied). We simulated high-resolution data using a PPP$= 10$ photons and SBR$= 1$ and then applied the downscaling and blur operations as in (5). Fig. 2 shows the obtained point-cloud, and the corresponding blurring kernels (see top-right). This figure shows sparse point-cloud with multiple outliers when considering the classical algorithm. The DS3D shows cleaner point clouds, and better features. Fig. 3 shows the equivalent depth images for uniform blur kernel highlighting better reconstructions of small objects/features.

## V. Results on real data

We evaluate DS3D on real data acquired in extreme conditions and provided in [13]. We focus on the elephant scene which comprises a $256 \times 256 \times 1536$ histogram and

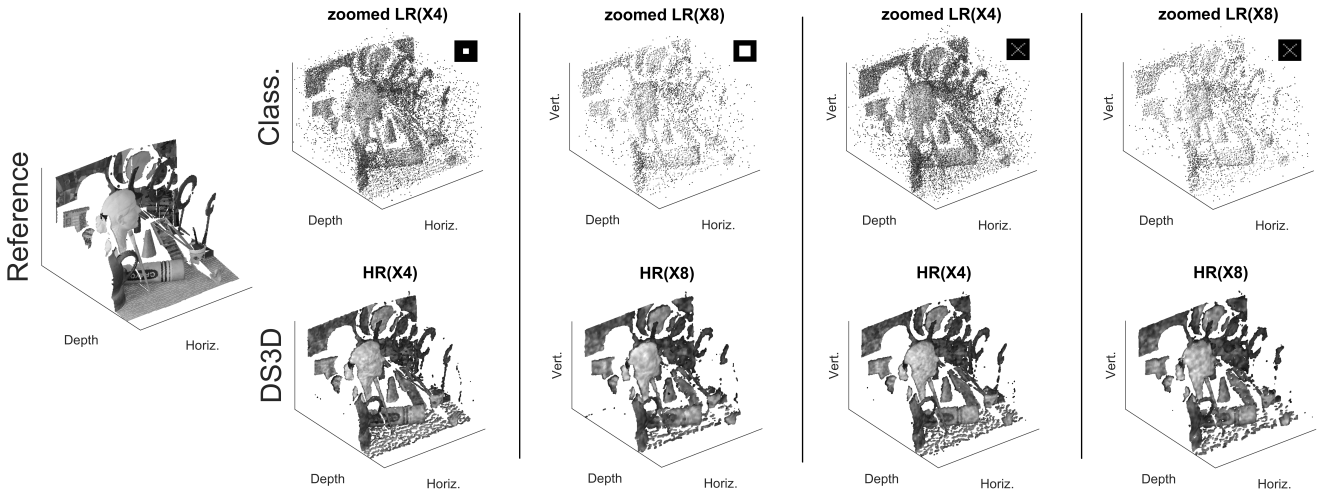


Fig. 2. 3D reconstructions of the art scene with (top row) the classical and (bottom row) DS3D algorithms. The two first columns show uniform blurring kernel, and column three and four an arbitrary kernel. The SR scaling factor is indicated in the subplot titles.

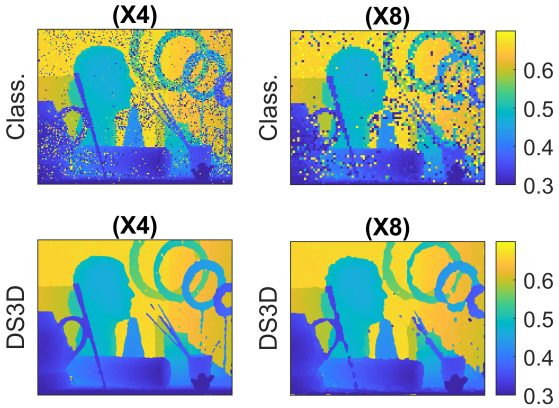


Fig. 3. Depth maps for (top) the classical and (bottom) the DS3D algorithms when applied to low resolution images with uniform blur kernels.

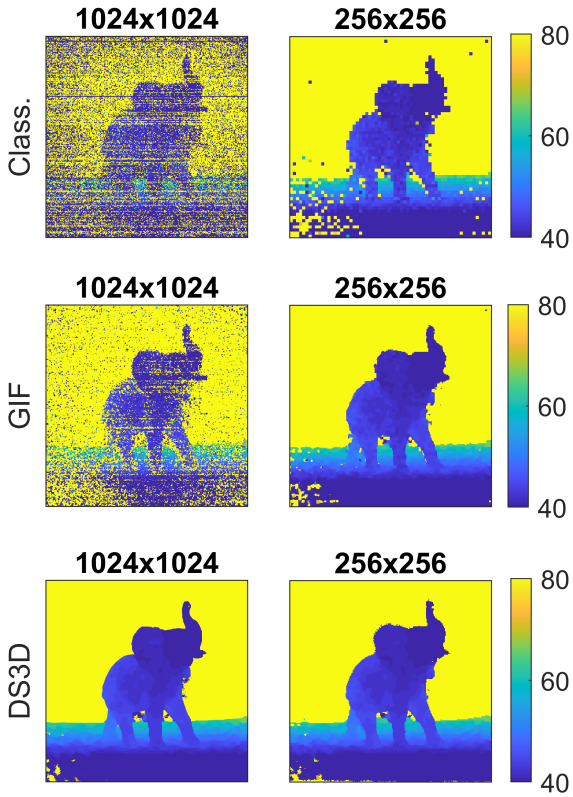


Fig. 4. Reconstructed depth maps for the DS3D x4 algorithm on real data. (Left) $1024 \times 1024$ image, (right) $256 \times 256$ image.

a $1024 \times 1024$ reflectivity image used as a guide. We also compare with GIF when applied to filter the histogram of counts followed by a depth estimation as in (3). Fig. 4 (left column) presents the reconstructed depth maps with the classical, GIF and DS3D algorithms, highlighting cleaner results for the latter. To further evaluate the SR capabilities of DS3D, we have also downsampled the data to $64 \times 64 \times 1536$ histogram and a $256 \times 256$ reflectivity and applied DS3D $\times 4$. Fig. 4 (right column) confirms the good results of DS3D.

## VI. Conclusions

This paper has presented a new plug-and-play method for joint depth deblurring and super-resolution. The method can be easily used with different downscaling factors and arbitrary blur kernels. The guided image filtering [18] algorithm was used to deliver analytical iterative steps, resulting in an efficient estimation. Results indicated good denoising, super-resolution and deblurring performance. Future work will consider other deep-learning guiding filters, and generalizations to high-dimension super-resolution (3D videos, multispectral 3D imaging).

## REFERENCES


[1] A. M. Wallace, A. Halimi, and G. S. Buller, "Full waveform lidar for adverse weather conditions," *IEEE Trans. Vehicular Tech.*, vol. 69, no. 7, pp. 7064–7077, 2020.

[2] J. Rapp, J. Tachella, Y. Altmann, S. McLaughlin, and V. K. Goyal, "Advances in single-photon lidar for autonomous vehicles: Working principles, challenges, and recent advances," *IEEE Signal Process. Mag.*, vol. 37, no. 4, pp. 62–71, 2020.

[3] G. Satat, M. Tancik, and R. Raskar, "Towards photography through realistic fog," in *2018 IEEE International Conference on Computational Photography (ICCP)*, 2018.

[4] A. Halimi, A. Maccarone, R. Lamb, G. S. Buller, and S. McLaughlin, "Robust and Guided Bayesian Reconstruction of Single-Photon 3D Lidar Data: Application to Multispectral and Underwater Imaging," *IEEE Trans. on Comput. Imaging*, vol. 7, pp. 961–974, 2021.

[5] R. Tobin, A. Halimi, A. McCarthy, P. J. Soan, and G. S. Buller, "Robust real-time 3D imaging of moving scenes through atmospheric obscurant using single-photon LiDAR," *Sci Rep*, vol. 11, no. 1, p. 11236, 2021.

[6] A. M. Pawlikowska, A. Halimi, R. A. Lamb, and G. S. Buller, "Single-photon three-dimensional imaging at up to 10 kilometers range," *Opt. Express*, vol. 25, no. 10, pp. 11 919–11 931, May 2017.

[7] J. Rapp and V. K. Goyal, "A Few Photons Among Many: Unmixing Signal and Noise for Photon-Efficient Active Imaging," *IEEE Trans. Comput. Imaging*, vol. 3, no. 3, pp. 445–459, 2017.

[8] J. Tachella, Y. Altmann, N. Mellado, A. McCarthy, R. Tobin, G. S. Buller, J.-Y. Tourneret, and S. McLaughlin, "Real-time 3D reconstruction from single-photon lidar data using plug-and-play point cloud denoisers," *Nat. Commun.*, vol. 10, no. 1, 2019.

[9] A. Halimi, R. Tobin, A. McCarthy, S. McLaughlin, and G. S. B. Buller, "Restoration of multilayered single-photon 3d lidar images," in *2017 25th European Signal Processing Conference (EUSIPCO)*, 2017, pp. 708–712.

[10] A. Halimi, R. Tobin, A. McCarthy, J. Bioucas-Dias, S. McLaughlin, and G. S. Buller, "Robust restoration of sparse multidimensional single-photon LiDAR images," *IEEE Trans. Comput. Imaging*, vol. 6, pp. 138 – 152, 2019.

[11] J. Peng, Z. Xiong, X. Huang, Z.-P. Li, D. Liu, and F. Xu, "Photon-Efficient 3D Imaging with A Non-local Neural Network," in *European Conference on Computer Vision (ECCV)*, 2020.

[12] Z. Sun, D. B. Lindell, O. Solgaard, and G. Wetzstein, "Spadnet: deep rgb-spad sensor fusion assisted by monocular depth estimation," *Opt. Express*, vol. 28, no. 10, pp. 14 948–14 962, May 2020.

[13] D. B. Lindell, M. O'Toole, and G. Wetzstein, "Single-photon 3d imaging with deep sensor fusion," *ACM Trans. Graph.*, vol. 37, no. 4, pp. 113:1–113:12, July 2018.

[14] A. Ruget, S. McLaughlin, R. K. Henderson, I. Gyongy, A. Halimi, and J. Leach, "Robust super-resolution depth imaging via a multi-feature fusion deep network," *Opt. Express*, in press.

[15] T. Seets, A. Ingle, M. Laurenzis, and A. Velten, "Motion adaptive deblurring with single-photon cameras," in *Proceedings of the IEEE/CVF Winter Conference on Applications of Computer Vision*, 2021, pp. 1945–1954.

[16] Z.-P. Li, X. Huang, P.-Y. Jiang, Y. Hong, C. Yu, Y. Cao, J. Zhang, F. Xu, , and J.-W. Pan, "Super-resolution single-photon imaging at 8.2 kilometers," *Opt. Express*, vol. 28, no. 3, pp. 4076–4087, Feb 2020.

[17] S. V. Venkatakrishnan, C. A. Bouman, and B. Wohlberg, "Plug-and-play priors for model based reconstruction," in *2013 IEEE Global Conference on Signal and Information Processing*, 2013, pp. 945–948.

[18] K. He, J. Sun, and X. Tang, "Guided image filtering," *IEEE Transactions on Pattern Analysis and Machine Intelligence*, vol. 35, no. 6, pp. 1397–1409, June 2013.

[19] Q. Legros, J. Tachella, R. Tobin, A. Mccarthy, S. Meignen, G. S. Buller, Y. Altmann, S. Mclaughlin, and M. E. Davies, "Robust 3d reconstruction of dynamic scenes from single-photon lidar using beta-divergences," *IEEE Trans. Image Process.*, vol. 30, pp. 1716–1727, 2021.

[20] A. Papoulis and S. U. Pillai, *Probability, Random Variables and Stochastic Processes*. McGraw Hill Higher Education, 2002.

[21] R. Tobin, A. Halimi, A. McCarthy, P. Soan, and G. Buller, "Robust real-time 3d imaging of moving scenes through atmospheric obscurants using single-photon lidar," *Optica*, 2021, submitted.

[22] I. Gyongy, S. W. Hutchings, A. Halimi, M. Tyler, S. Chan, F. Zhu, S. McLaughlin, R. K. Henderson, and J. Leach, "High-speed 3d sensing via hybrid-mode imaging and guided upsampling," *Optica*, vol. 7, no. 10, pp. 1253–1260, Oct 2020.

[23] D. Ulyanov, A. Vedaldi, and V. Lempitsky, "Deep image prior," in *Proceedings of the IEEE conference on computer vision and pattern recognition*, 2018, pp. 9446–9454.

[24] K. Zhang, L. V. Gool, and R. Timofte, "Deep unfolding network for image super-resolution," in *Proceedings of the IEEE/CVF Conference on Computer Vision and Pattern Recognition (CVPR)*, June 2020.

[25] N. Zhao, Q. Wei, A. Basarab, N. Dobigeon, D. Kouamé, and J.-Y. Tourneret, "Fast single image super-resolution using a new analytical solution for $\ell_2 - \ell_2$ problems," *IEEE Transactions on Image Processing*, vol. 25, no. 8, pp. 3683–3697, 2016.

[26] H. Hirschmuller and D. Scharstein, "Evaluation of cost functions for stereo matching," in *IEEE Conference on Computer Vision and Pattern Recognition (CVPR)*, 2007.

[27] J. Rapp and V. K. Goyal, "A few photons among many: Unmixing signal and noise for photon-efficient active imaging," *IEEE Trans. Comput. Imaging*, vol. 3, no. 3, pp. 445–459, Sept. 2017.